Article

Investigation of the Causes of Premature Rain Erosion Evolution in Rotor Blade-like GFRP Structures by Means of CT, XRM, and Active Thermography

Friederike Jensen [1,*], Elie Abi Aoun [2], Oliver Focke [2], Andreas Krenz [3], Christian Tornow [3], Mareike Schlag [3], Catherine Lester [4], Axel Herrmann [2,5], Bernd Mayer [3,5], Michael Sorg [1] and Andreas Fischer [1]

[1]   Bremen Institute for Metrology and Quality Science (BIMAQ), University of Bremen, Linzer Str. 13, 28359 Bremen, Germany
[2]   FIBRE—Faserinstitut Bremen e.V., University of Bremen, Am Biologischen Garten 2, 28359 Bremen, Germany
[3]   Fraunhofer Institute for Manufacturing Technology and Advanced Materials IFAM, 28359 Bremen, Germany
[4]   Fraunhofer Institute for Wind Energy Systems IWES, 27572 Bremerhaven, Germany
[5]   Faculty for Production Engineering, University of Bremen, Bibliothekstraße 1, 28359 Bremen, Germany
*   Correspondence: f.jensen@bimaq.de

Abstract: Premature rain erosion damage development at the leading edges of wind turbine rotor blades impair the efficiency of the turbines and should be detected as early as possible. To investigate the causes of premature erosion damage and the erosion evolution, test specimens similar to the leading edge of a rotor blade were modified with different initial defects, such as voids in the coating system, and impacted with waterdrops in a rain erosion test facility. Using CT and XRM with AI-based evaluation as non-destructive measurement methods showed that premature erosion arises from the initial material defects because they represent a weak point in the material composite. In addition, thermographic investigations were carried out. As it shows results similar to the two lab-based methods, active thermography has a promising potential for future in-situ monitoring of rotor blade leading edges.

Keywords: rain erosion; rotor blade leading edge; damage evolution; X-ray computed tomography; X-ray microscopy; active thermography; artificial intelligence

1. Introduction

The progressive development of even larger wind turbines due to the continuously growing demand for wind power, an important renewable energy technology, results in increased tip speeds at the leading edges of modern rotor blades. With this development, the damage potential and impact of rain erosion have also increased [1]. Rain erosion damage to the rotor blade surface reduces performance and affects the lifetime of wind turbines [2]. Accordingly, rain erosion is an important aspect to be considered in wind turbine operation. The current assumptions about failure mechanisms due to manufacturing defects in material, coatings [3], and the interface [4,5] need to be reduced to increase the understanding of rain erosion. Rain erosion damage on the leading edge of a wind turbine rotor blade has already been investigated. For example, a guideline to qualify glass fiber-reinforced plastic (GFRP) coating systems for rotor blade applications was developed [3]. It is based on test specimens that were manufactured and eroded in the erosion test rig, and the damage was subsequently evaluated using destructive measuring methods, e.g., micrograph analyses. The test specimen condition before rain loading was not considered but can be essential for the occurrence of erosion damage in many cases. Although this guideline-compliant approach succeeds in distinguishing between different coating systems in terms of their performance, no validated theories to date explain the formation mechanisms of erosion

damage. Moreover, it does not allow any statement to be made regarding the expected time course of the damage progress. However, this is important for enabling the early detection of the damage and assessing the damage with respect to the decision and planning of a repair.

In recent years, X-ray computed tomography (CT) has found wide application in materials science research [6–8]. Furthermore, the determination of fiber orientation in short fiber injection molded components [9] using CT is of great importance, as well as the use and analysis of in-situ experiments for a deeper understanding of the failure mechanisms of fiber-reinforced wind turbine blades. A cyclic study performed by Nash [10] investigated the degradation of plate-like fiberglass composite structures in an erosion test rig. An evaluation of the degradation was carried out using CT examinations and analyses. The removal of the coating between the individual cyclic loads was determined using a voxel size of 14.8 μm^3 (Nikon XT H 225 LC X-ray system). Mishnaevsky [11] studied a 2 cm^3 section of a wing leading edge stressed in a rain erosion test rig that was inspected by scanning electron microscopy and X-ray microscopy (XRM, Zeiss Xradia 520 Versa). The specimen examined included intact as well as damaged areas. With a voxel size of 2 μm^3, the defects were detected and documented by XRM. The data formed the basis of computer-aided micromechanical modeling of the effect that structure and coating properties have on rotor blade leading edge degradation. A causal analysis of the degradation was based on this simulation. However, all of these select systematic studies do not contain any early detection or time tracking of damage and failure due to rain erosion, so the failure mechanisms are not yet fully understood [4]. In conclusion, intimate material damage has not been considered in a specific and repeatable way, so the relationship between the initial condition of the specimens prior to erosion exposure and the damage patterns that occur after erosion exposure has not yet been investigated.

Lately, the use of artificial intelligence (AI) for the automated evaluation of large data sets is becoming crucial. In the field of engineering, the methods of deep learning could be applied to defect detection and differentiation in GFRP components. This requires datasets of CT slices, which are divided into training, testing, and validation datasets. In addition, deep learning tools such as "Data Augmentation" and "Transfer Learning" are used to facilitate the iterative learning of the algorithm. Banga et al. combined thermography tests with deep learning techniques in order to detect cracks [12]. Badran et al. used convolutional neural networks (CNN) to distinguish phases from shape and edge information rather than intensity differences and successfully segment phases in a unidirectional composite that also had a coating with similar image intensity [13]. In fact, such algorithms are also suitable for defect detection. These neural networks use folding layers to detect the different features of an image, such as edges, corners, and lines. The open-source nature of deep learning offers an ever-growing online community that allows access to established neural networks such as U-Net [14].

Since rain erosion on wind turbine blades has to be investigated in the open field at the turbine itself, there is a need for a measurement technique for in-situ inspections. Active thermography is a non-destructive measurement method for detecting defects close to the surface. Unlike CT and XRM, it can be used in the open field for in-situ measurements. Previous studies have already shown good suitability for defect detection in rotor blade leading edge-like specimens, where the defects were simulated by drilling holes from the back side of the specimens [15]. The extent to which realistic defects can be detected, such as trapped air bubbles, which have different properties than inserted borings, has not yet been investigated. With regard to the visualization and observation of damage growth, several thermographic investigations have already been successfully carried out on partially pre-damaged test specimens made of fiber-reinforced composites with different loads. Colombo et al. performed thermographic studies on GFRP plates pre-damaged with delaminations and observed the damage growth under tensile loading [16]. Thermographic imaging of impact damage to GFRP plates caused by impacts with different hammers in a drop-weight testing machine was performed by Katunin et al. [17]. Meola

et al. also thermographically investigated the impact damage on GFRP sheets, which were pre-damaged by production defects such as porosity during hand lamination prior to impact loading [18]. All studies show that thermography can be used to visualize the condition of a pre-damaged or undamaged fiber-reinforced composite plate before and after different impacts and to document the damage growth that occurred. However, the detection capabilities of thermography with respect to damage growth beginning with a realistic sub-surface defect in a rotor-blade-leading-edge-like test specimen up to the surface damage—as it occurs on wind turbines in operation due to the exposure to rain—need to be identified.

This work aims to clarify whether damage that is close to reality can be produced in the laboratory and whether it induces surface damage under a rain load. It will also address the lack of correlation between the condition before and after erosion in order to enable the prevention and early detection of incipient erosion. To achieve this goal, defined initial defects are introduced into rotor-blade-leading-edge-like test specimens, which are then subjected to loading in a rain erosion test facility. The test specimens are analyzed in the initial state and after the rain loading using XRM, CT, and an imaging surface analytical method. Thermographic investigations are carried out as a feasibility study for in-situ measurements at the rotor blade leading edge. In addition, the resolution of the current damage state will be clarified and, thus, the visualization, detection, and differentiation of the defects below and on the surface of rotor-blade-leading-edge-like specimens after rain exposure.

Note that erosion protection concepts based on films will not be investigated within the scope of this work, as these systems have not played a relevant role in practical applications due to unresolved processing and application challenges.

2. Materials and Methods

2.1. Preparation of the Test Specimens

For the investigations, a single base type of test specimen is manufactured, and different kinds of initial defects are introduced. The basic structure of the specimen is adapted from a real rotor blade leading edge with a laminated GFRP half tube as a supporting structure. On the GFRP, filler and coating are applied, as shown in Figure 1.
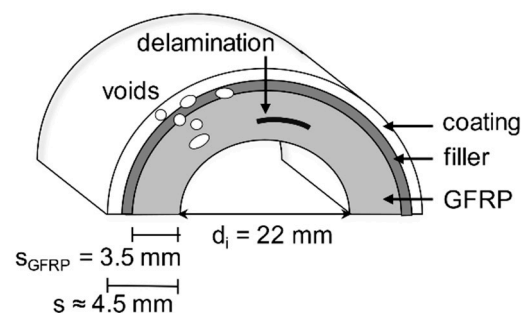

Figure 1. Schematic representation of the basic specimen structure with the modification of individual layers.

To recreate realistic rotor-blade-leading-edge-like specimens, different defects such as voids and delaminations are introduced into different layers of the test specimen, labeled in the following with the corresponding letter from Table 1. The GFRP test specimens were manufactured using the vacuum infusion process. The laminate structure on the specimen surface is $\pm 45°$ with a structure of the scrim (surface) as biaxial, biaxial, unidirectional, and biaxial. The specific gravity of the fibers is biaxial 830 g/m^2 and unidirectional 990 g/m^2 with a fiber volume content between 50% and 55%. The resin system used was RIM 135 with hardener type: RIM 137 from Hexion.

Table 1. Overview of the different test specimen modifications.

Sign	Modification	Introduction Method of the Modification
L	Voids in GFRP	Introduction by air intake during GFRP lamination
D	Delamination in GFRP	Introduction by Teflon film between individual laminate layers
B	Voids in coating	Introduction of styrofoam balls withing the coating
S	Voids in filler	Introduction of styrofoam balls withing the filler
R	Reference specimen	No explicitly introduced initial defects

The voids in the GFRP composite material (**L**) were introduced during the production of the test specimens in the vacuum process. In this process, undefined defects were generated in the GFRP specimen in terms of localization and shape, as they can also occur in the real manufacturing process, see Figure 2a.
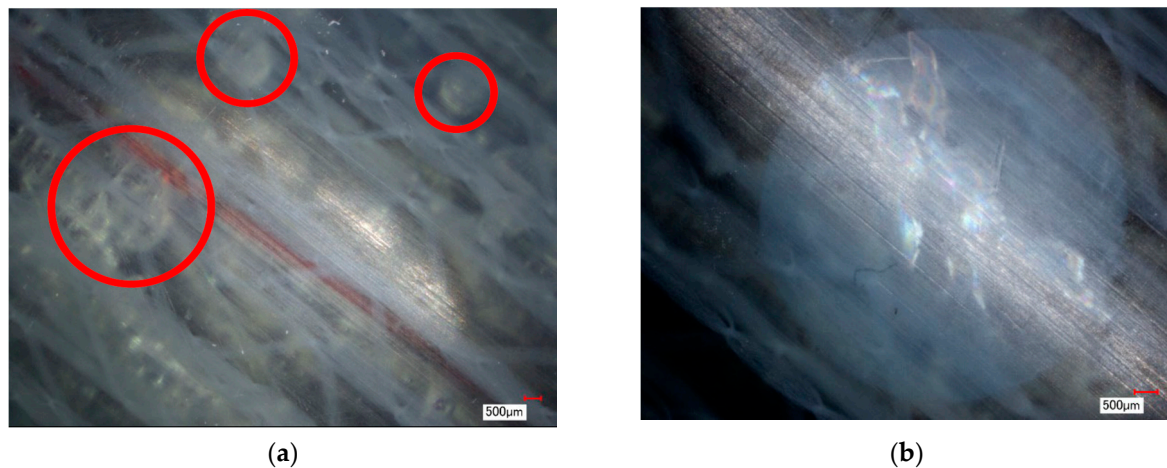

(**a**)   (**b**)

Figure 2. Photograph of part of the GFRP specimen with initial defects as (**a**) introduced voids (within the red circle) and (**b**) introduced delamination, adapted with permission from [19].

The delaminations in the GFRP composite material (**D**) were already introduced during the layer-by-layer buildup of the GFRP test specimen. For this purpose, round Teflon foil cutouts with a diameter of 7 mm–10 mm were positioned at defined points between the GFRP layers, see Figure 2b. The Teflon foil provides local debonding between the individual fiber layers. The styrofoam balls for imitating voids in the coating system (S) have a diameter of ~ 1 mm ± 0.4 mm and were introduced manually directly during the coating process of the filler, see Figure 3. Due to the electrostatic properties of the styrofoam balls, they had to be adhered to the specimen surface using a thin underlayer. This underlayer was applied as thinly as possible to the putty material using a flexible comb. On top of the underlayer with applied styrofoam balls, a covering layer of the putty material was applied. After a sufficiently long drying time, the putty was ground off mechanically to produce the geometrically correct shape of the specimens and to generate a sufficiently rough surface in preparation for the coating of the specimens afterward.

The introduction of voids in the coating (**B**) was carried out with the same styrofoam balls, which were first positioned on an undercoat (on top of the putty) of the material applied as thinly as possible before, in the next step, the test specimens including the applied styrofoam balls were poured with coating. Note that the specimen with the applied styrofoam balls in the coating had to be overpoured with several layers to completely cover the applied styrofoam balls. Therefore, the specimens with this initial defect have a significantly higher coating thickness compared to the other specimens.

Figure 3. Introduction of the styrofoam balls (**a**) within the filler, adapted with permission from [19] and (**b**) on the filler layer within the coating.

2.2. Cyclic Rain Loading Tests

In order to investigate the effects of initial defects on early rain erosion, the manufactured test specimens have to be impacted by rain. The specimens were tested in the Fraunhofer IWES' Leading Edge Lab, shown in Figure 4. The helicopter-style test facility contains a rotating disc of 2 m in diameter, in which three test specimens of 236 mm length are installed and can spin up to 120 m/s at the outer tip of the specimen. Then, four rain tanks introduce water droplets 3 m above the test specimen. After a defined test interval, the specimens were inspected.
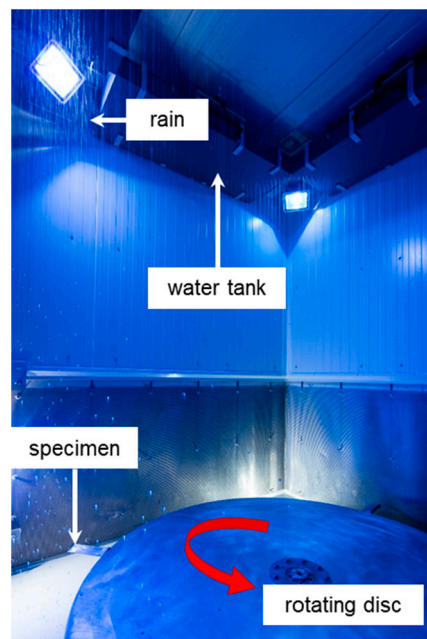

Figure 4. Photo of the inside of the IWES rain erosion test facility.

Thereby, the rain erosion system parameters were designed to be as close to reality as possible. However, since damage progress under real conditions only occurs after a very long period of time, the parameters of the test facility were adjusted so that initial erosion damage occurs in an acceptable time of a few hours. The times at which erosion damage occurs vary depending on the coating system and the condition of the specimen, e.g., initial defects. With the parameters from Table 2, erosion damage could be generated within 4 h of rain loading on a specimen with introduced defects in the form of voids in the coating. The specified test parameters and the IWES test facility fit within the DNV-GL (Det Norske Veritas and Germanischer Lloyd, classification society) recommended practice [20].

Table 2. Overview of the parameter settings of the rotating rain erosion test facility.

Parameter Settings	
rotation speed	120 m/s
drop size	1–2 mm
rain intensity	20 L/min
ambient temperature	23 °C

Figure 5 shows specimens installed in the holders and examples of rain erosion damage.
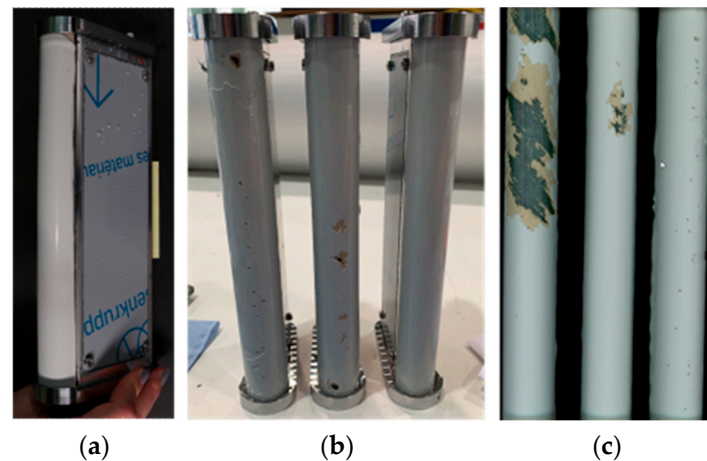

| (a) | (b) | (c) |

Figure 5. (**a**) Clamped specimens before rain erosion testing, (**b**) clamped specimens in between rain erosion testing, and (**c**) specimens after rain erosion testing, adapted with permission from [19].

2.3. Analysing Methods

2.3.1. XMR and CT with Artificial Intelligence Evaluation

For the investigation of the inner structure of the specimens, CT and XRM are commonly used non-destructive measuring methods; see Figure 6.
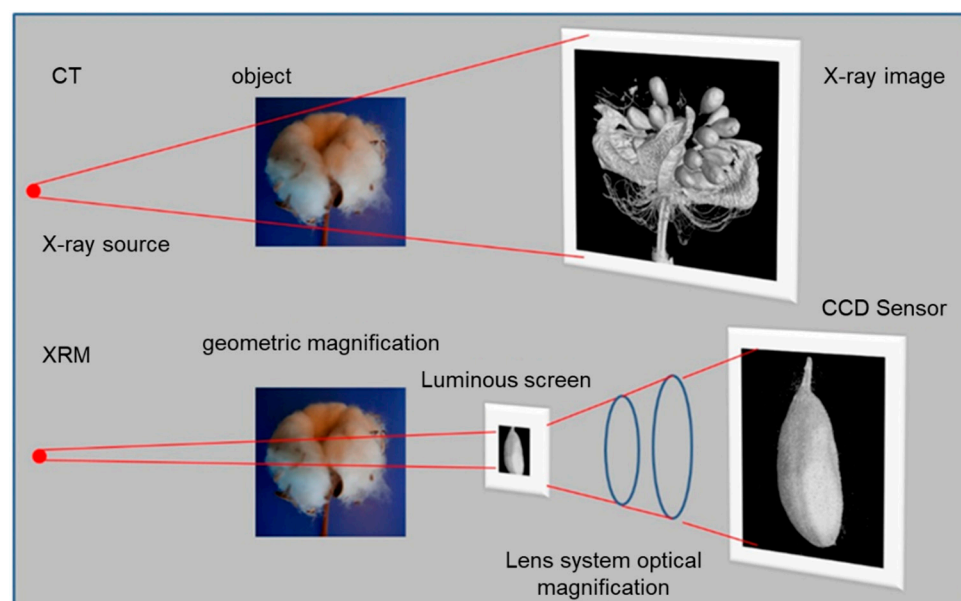

Figure 6. Schematic structure of the X-ray techniques: CT: geometric magnification, the object must be placed close to the source and reduced in size for a maximum magnification, XRM: geometric and optical magnification, using a cotton ball and seeds as examples, a reduction of the object is not necessary.

In contrast to the conventional μ-CT, the XRM uses a two-stage magnification technique based on synchrotron caliber optics [8,9]. The geometrically enlarged projection is further magnified using a scintillator layer that converts X-rays into visible light, which can then be optically magnified using different objectives mounted to a microscope turret. The two-stage setup provides *Resolution at a Distance*, allowing large, flexible working distances while maintaining submicron resolution (spatial resolution < 700 nm) without the need to downsize the specimen. Figure 7a shows an example for an initial overview XRM scan capturing an $(28 \times 30 \times 2)$ mm^3 glass fiber-reinforced object. A cross-sectional image by using a 0.4× magnification optic where the pixel size is 32 μm is shown in Figure 7b.
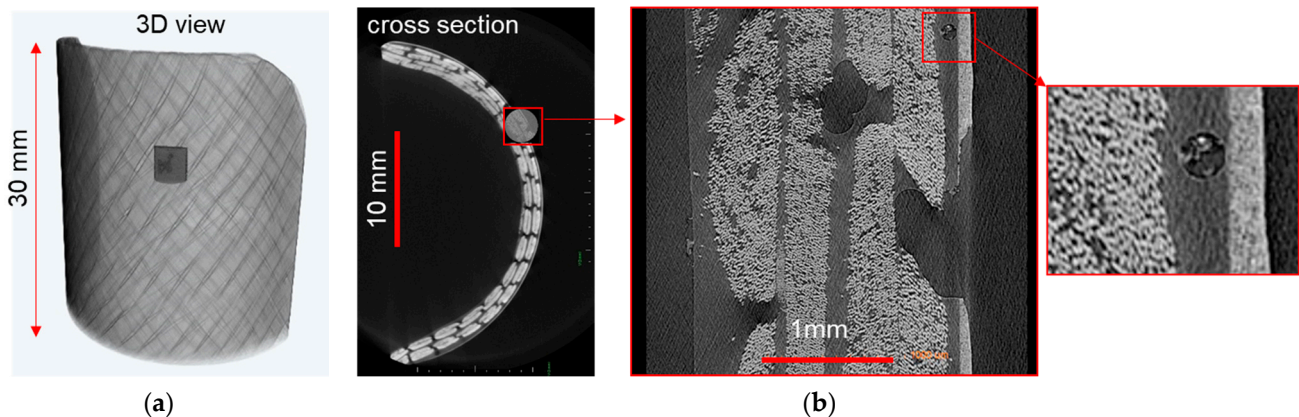

Figure 7. XRM-scans: (**a**) 3D view of the whole object, (**b**) cross-sectional image with ROI, ROI-scan as a sectional view, ROI with pore [19].

Once a region of interest (ROI) is determined, the distances between the source, object, and detector along the optical axis are adjusted according to the desired magnification. In addition, the component perpendicular to the optical axis (source-detector) can be adjusted so that the ROI remains on the optical axis during component rotation. The second scan captures a volume of $2.8 \times 3 \times 1.8$ mm^3 when using the lens with a 4× magnification (Figure 7b). Here, the pixel size decreases to 2 μm. In the digital enlargement of the scan, the four glass fiber layers, the matrix, the filler layer, and a pore can be seen.

The data generated by μ-CT is of large scale. With around 2000 cross-sectional images per scan, split images obtained from CT measurements require an efficient data processing scheme because the manual search for defects in a scan made of several slices is time-consuming. Therefore, machine and deep learning were applied as a means to locate defects in the specimens. Deep learning segmentation requires graphical computing power, which in this project was provided by an NVIDIA Quadro M5000 with 8 GB of GPU memory. It was capable of supporting CNN models up to 8,593,350 parameters. The defects in this work are mainly styrofoam spheres, modeling voids in the coating and/or filler layer, and glass fiber-reinforced laminate. The primary challenge limiting the success of AI for engineering applications is the availability of labeled data sets. Such labeled data is needed to train the neural network. For this reason, the first step towards automated data processing using AI is to generate meaningful labeled data. The labeling was done using the segmentation wizard [21], an image processing software. ORS Dragonfly [22] was used to generate the virtually labeled data for training, and the built-in untrained neural networks were used. A virtual rectangular white frame shown in Figure 8 represents a part of the specimen within a black background. A coating layer, filler layer, glass fiber-reinforced laminate, a surplus of the matrix, and a void in the coating layer are enclosed by the frame. A few pixels of each material layer, the background, and the defect were manually labeled with different colors, as seen in Figure 8a. Then machine learning was adopted to avoid the manual labeling of all the pixels. Here, a random forest classifier based on a decision tree delivered the segmentation of the to-be labeled frame in Figure 8b. The adjusted random forest prediction delivers enough labeled pixels to start training a neural network.

Convolutional neural networks (CNN) are standard deep learning tools in the field of image processing. An established neural network for semantic image segmentation is the U-Net [14], here for the automated defect detection in the specimen. The size of the images used for U-Net segmentation is 774 px × 1284 px × 2013 px (width/height/depth).

(a)   (b)
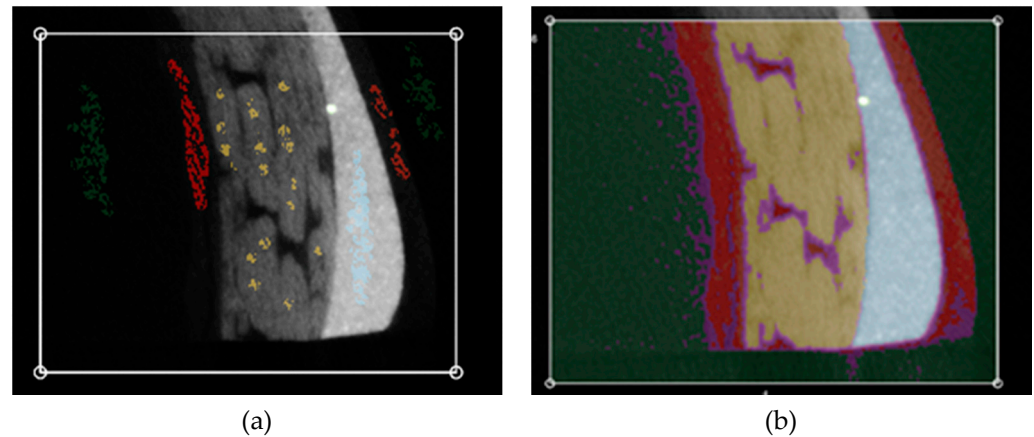
Figure 8. (**a**) Result of manual pixel-wise labeling of a CT-slice, (**b**) result of labeling of a virtual frame using a random forest classification [19].

The first training of the U-Net took 15 min and was done using two virtually labeled data sets, such as the one shown in Figure 8b. In total, the U-Net was trained 12 times and fed with a new virtually labeled frame for each training session, and 12 virtually labeled frames were used as the training data set. The training duration depended on the complexity of the labeled frames and varied between 15 and 72 min, averaging 30 min per/training. The training of the neural network consists of adjusting the values of the weights epoch-wise using gradient descent, with the objective being error minimization. Here, the epoch refers to one cycle through the full training dataset. In an epoch, an entire dataset is passed forward and backward through the neural network only once. Usually, training a neural network takes more than a few epochs. The evolution of the loss function during the first training (where only two virtually labeled frames were used) is shown in Figure 9.
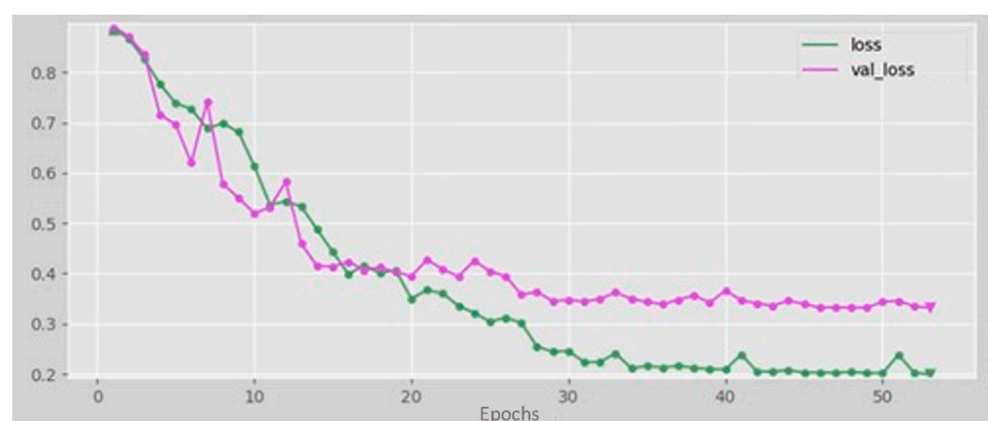

Figure 9. Loss function vs. epochs during the first U-Net training [19].

Loss functions decrease with time, i.e., with an increasing number of epochs (which are training cycles made out of several batches). The first training did not deliver the required weights of the CNN to successfully segment all CT slices and locate all defects, which is indicated by efficient training. Note the drop of the green curve (loss function) with time, i.e., with the training evolution. For this reason, additional training was needed.

Figure 10 shows the evolution of the loss training after the final (10th) training of the U-Net.
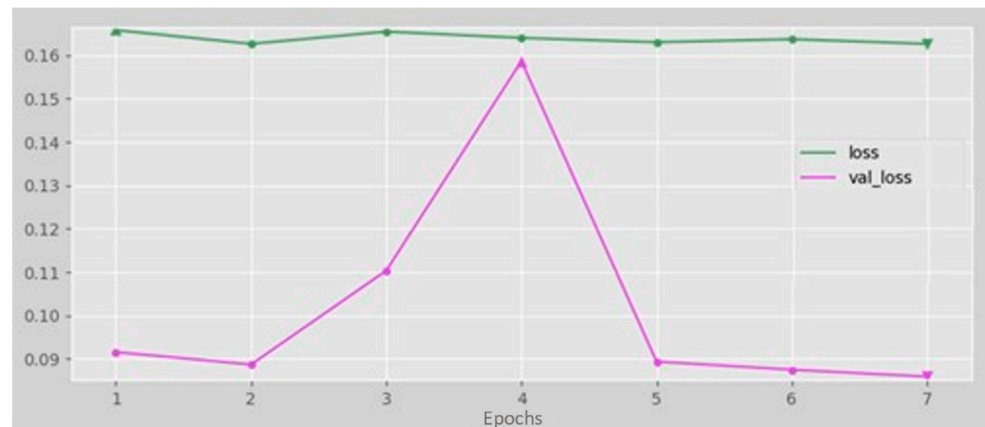
Figure 10. Loss function after the last U-Net training [19].

The reduction of the loss function stagnated (0.163) after the 10th training. An error minimization from 0.9 after the first training to 0.163 after the last training was attained, and further training was not beneficial. Since the difference between the validation loss function and loss function is partially less than 0.05, no conclusion regarding overfitting or underfitting of the neural network could be made. The success of distinguishing between different material layers can be seen in Figure 11a.
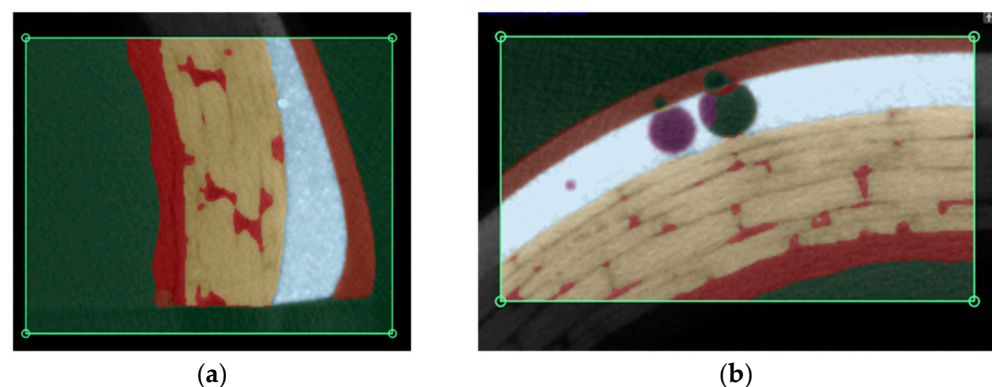

(**a**)   (**b**)

Figure 11. Automatic segmentation of the virtual images using the U-Net CNN in the Segmentation Wizard, adapted with permission from [21].

A greater challenge was the identification of pores (in purple, Figure 11b). The small pores were fully detected, while the larger ones were only partially detected. It was also found that the air bubbles in the coating, located above the pores in the filler layer, were not detected. However, the obtained results did not improve with further training. For this reason, a Sensor 3D [23] CNN with a different architecture was investigated to obtain better results.

2.3.2. 3D Surface Analysis

The fringe light projection method is an optical measurement method for the three-dimensional detection of surfaces. The surface to be measured is illuminated sequentially at a defined angle with a pattern of light and dark stripes of different widths. Cameras capture the projected fringe patterns from the captured temporal sequence of different brightness values for the individual pixels, the underlying three-dimensional surface topography of the captured object. The geometry of the detected surface is resolved in the μm range. The measurements are carried out with a 3D profilometer of the type VR-3200 from the manufacturer Keyence. For the evaluation of the measurement data, a surface shape correction of the round specimen surface was applied in order to visualize the surface of the specimens and their influence by the rain erosion as optimally as possible.

2.3.3. Active Thermography

Long-pulse thermography belongs to the measuring methods of active thermography, in which the measured object is first excited with a heat source for a few seconds. Then the infrared radiation returned by the measured object is recorded using a thermographic camera, see Figure 12. The thermal excitation causes a material-specific heat flow in the measured object, resulting in characteristic surface temperature distribution. The infrared camera then visualizes this temperature distribution in the form of thermograms [24,25].
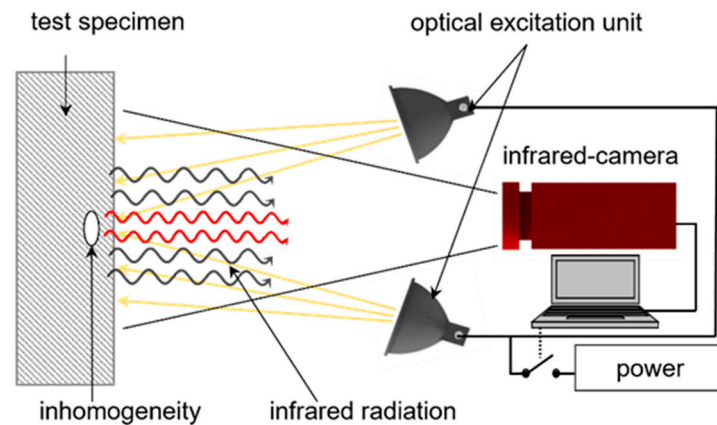

Figure 12. Schematic representation of the measuring principle of active thermography.

During measurement, the specimens are clamped in a test rig, see Figure 13. Then, kinematics are used to correctly position the specimen in front of the thermographic camera and the excitation unit, consisting of two halogen lamps. To avoid anomalies caused by the thermal reflections of the excitation unit onto the curved specimen, the excitation unit is positioned below and above the specimen. The two halogen lamps, each with a power of 1 kW, are placed at an angle of approximately 90° to each other and have a distance to the specimen of $k = 204$ mm.
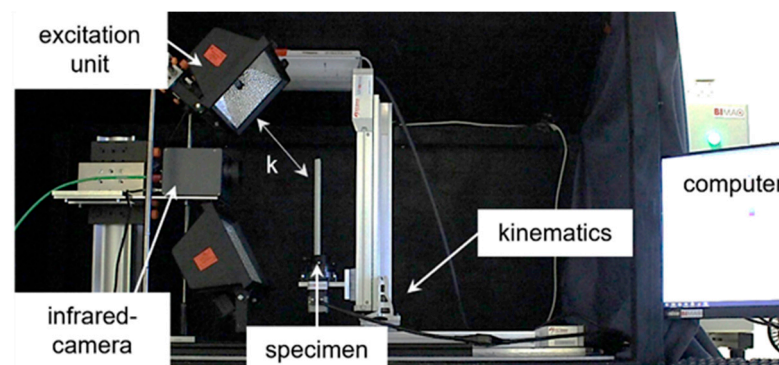

Figure 13. Photo of the experimental setup for clamping and examination of the specimens at a distance between the excitation unit and specimen of $k = 204$ mm.

Table 3 shows the excitation durations used, which differ depending on the type of defect and the specimen. Specimens that have defects deeper in the material must be excited for a correspondingly longer time since the heat must travel a longer path through the material from the surface to the defect and return. Thermographic imaging is performed with the VarioCam hr head from the company InfraTec, which has a temperature resolution of 0.035 K, an image format of 640 px $\times$ 480 px, and operates in a wavelength range of 7.5–14 μm. The frame rate is 10 Hz for a measurement duration of 30 s, so 300 images are available in total for the image evaluation. Table 4 summarizes the experimental parameters.

Table 3. Overview of the different excitation times of the respective test specimens.

Specimen with Defect Type	Excitation Time t_{exc} [s]
Reference without defects	20
Voids in the coating/filler	10
Voids in GFRP	30
Delaminations	30

Table 4. Overview of the experimental parameters used.

Experimental Parameters	
Excitation power	2 kW
Range of wavelet	7.5–14 µm
Thermal resolution	0.035 K
Image size	640 px $\times$ 480 px
Recording time	30 s
Recording frequency	10 Hz

For the evaluation of the measured images, the last image of the series is subtracted from all previous images at first so that constant influences are subtracted. The differential raw image with the highest contrast, i.e., the highest intensity difference between a defect and a defect-free area, is selected from the recorded image sequence. According to previous experiments, the image is located within the first 10 thermograms, corresponding to the first second of the measurement acquisition for the parameters used.

3. Results and Discussion

The results are divided into three subsections based on the research questions presented. First, it is investigated whether real defects such as voids can be produced in the laboratory. Then, the damage development of initial defects before and after exposure to rain is observed and analyzed. Finally, the feasibility study of active thermography as an alternative measurement method to CT and XRM takes place, including a technique comparison for validation. Due to the large number of tests undergone and hence generated data, the results are focused on a specimen with built-in voids in the coating layer (specimen Type B).

3.1. Analysis of the Initial Specimen State

Figure 14 shows the resulting images of a test specimen section with inserted voids in the initial state from the high-resolution XRM measurements. Styrofoam spheres were placed in the area of the filler where their imprints left circular structures of different diameters in the sectional images. The spherical structures only become visible in the 3D images. The voids can be analyzed according to position, size, sphericity, and size distribution in VolumeGraphics, or their volume can be visualized in color-coded form, see Figure 14b. However, the analysis is time-consuming, so deep learning methods were further used for data analysis.
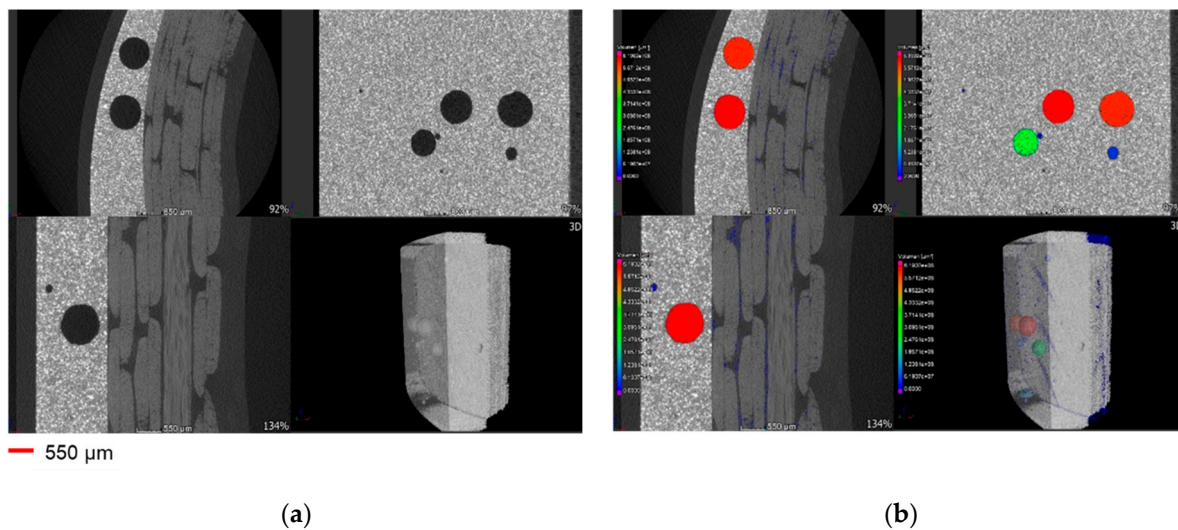
(**a**)

(**b**)

Figure 14. Image analysis on high-resolution XRM data of a specimen with voids in the filler. In (**a**) sectional images and 3D view in VoliumGraphics without analysis. In the area of the trowel application, there are particles with high density (bright dots) as well as artificially generated voids (dark circles) in the test specimen in (**b**) void analysis with color-coded volume sizes, adapted with permission from [19].

Figure 15 shows the results of the employed deep learning methods. In Figure 15a, one slice of the CT images is shown. The different layers of fibers and the filler are clearly visible. The void in the coating, the coating itself, and the resin of the GFRP laminate are barely visible due to their almost similar density. Therefore, the XMR data segmentation was done using U-Net (see Figure 15b. The U-Net was trained 12 times and an additional virtually labeled frame from different parts of the specimen was fed into the training data during each training. The average training duration was around 35 min. Since the results of the segmentation were inaccurate in the coating layer and did not ameliorate with further training, a Sensor 3D [25] CNN with a different architecture was examined for better results. The results using the Sensor 3D shown in Figure 15c were obtained after five training sequences, i.e., with five virtually labeled frames. Nevertheless, the training of the Sensor 3D is more time-consuming than that of the U-Net, with an average training duration of 68 min. The comparison of the achieved segmentation results using the U-Net and the Sensor 3D models depicts a clear advantage of the sensor 3D over the U-Net for the current purpose. The Sensor 3D CNN could not only differentiate between different material layers and the background, but the defects were also completely and correctly located.
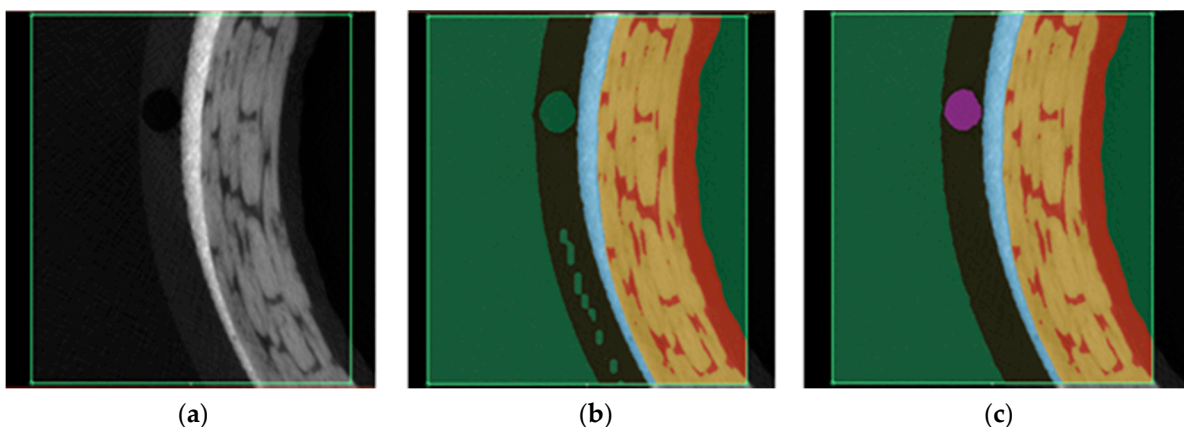

(**a**)

(**b**)

(**c**)

Figure 15. (**a**) CT slice (no. 303 out of 2014 images), (**b**) segmentation using U-Net, (**c**) segmentation using Sensor 3D [19].

In conclusion, manufacturing reproducible test specimens close to the structure and geometry of a real rotor blade leading edge and the inserted styrofoam balls in different coating system layers (filler and coating) to imitate voids was successful.

3.2. Analysis of the Erosion Evolution Using CT and XRM

In Figure 16, the 3D representation of the loaded specimen with three areas of different degrees of degradation in the filler layer is marked and shown in the left partial view (red circles).
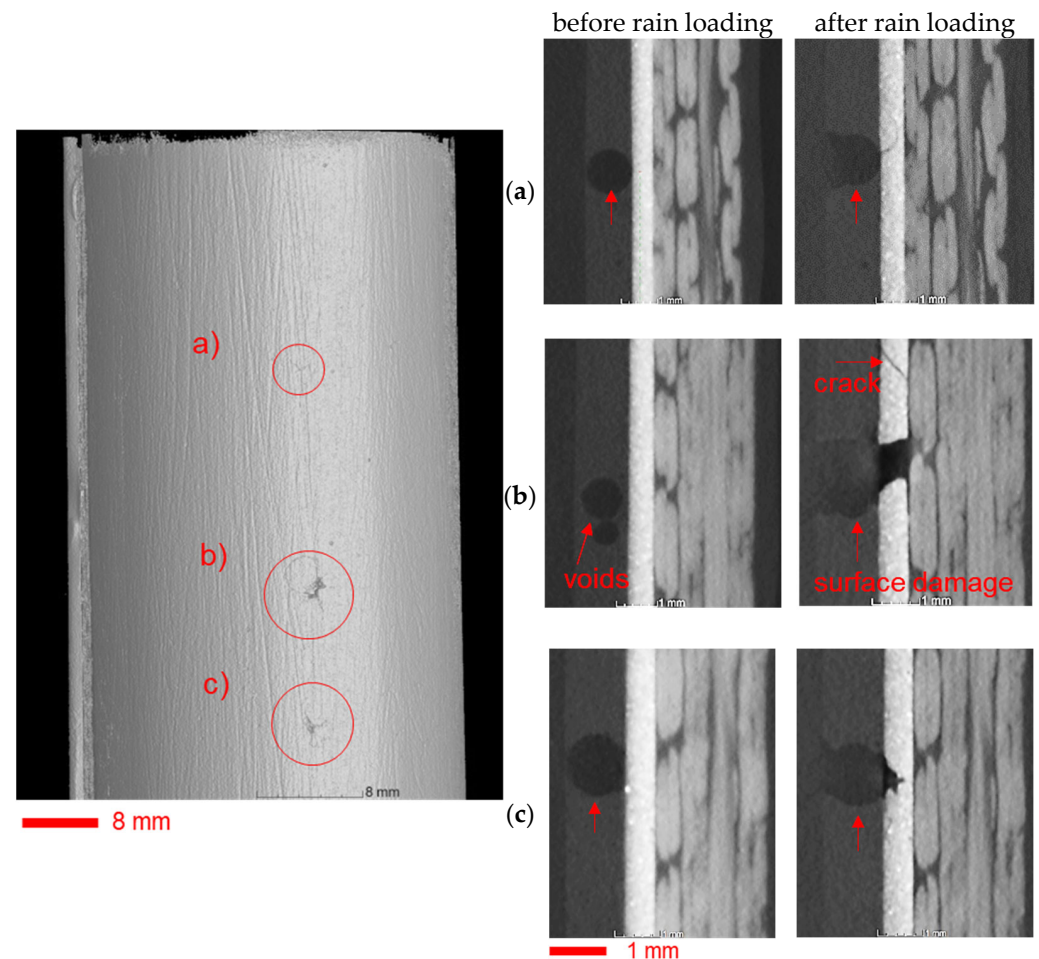

Figure 16. 3D representation of the loaded specimen (**left**) with marked positions (red circles) of the sectional view. The sectional views (**right**) show identical positions (**a**–**c**) before and after loading in the rain erosion test rig, adapted with permission from [19]. The red arrows mark voids in the GFRP, surface damage, or cracks in the material.

Corresponding sectional images showing the area before and after rain loading are shown on the right. Voids are present in the filler layer. It can be seen that the degree of degradation depends on the position of the pore, i.e., the distance to the air-coating layer interface, the size and number of voids, and the void volume. From the sectional images, a "time history" of the damage dynamics can be derived. At first, the coating layer gets broken and is therefore no longer present as protection of the filler, and cracks appear in the filler layer (Figure 16a). Second, the filler layer gets removed by abrasion or washed out (Figure 16c) until the GFRP structure is exposed (Figure 16b). Afterward, the bursting raindrops wash out the boundary layer between the GFRP and the filler, and cracks form outside the opening. The damage there is more extensive than the opening in the coating layer.

Figure 17 shows a cross-sectional view of the identical defect from Figure 16b at three different locations. Delamination can be seen along the interface between the GFRP and the filler (Figure 17a). The filler has been destroyed over a large area, and the extent is significantly greater than the opening in the coating layer (Figure 17b). A visual inspection of the defect from the outside would not capture the real extent of the destruction.
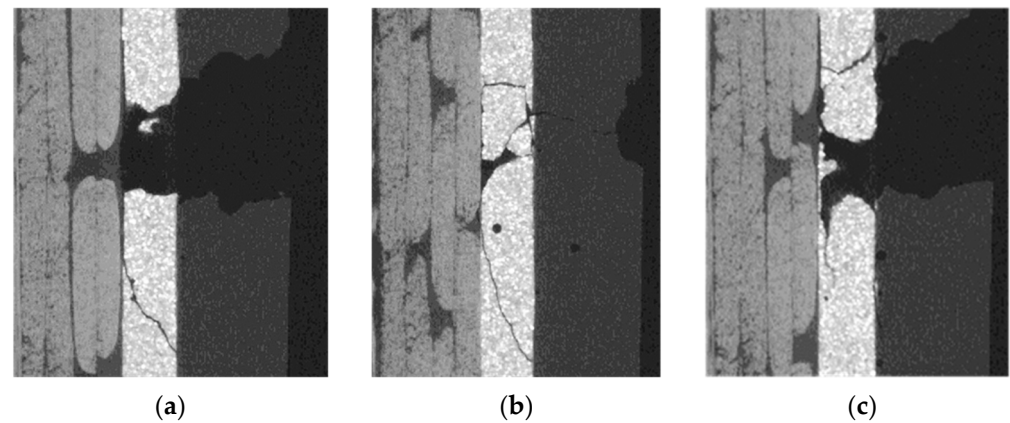

(**a**)   (**b**)   (**c**)

Figure 17. Cross-section of the identical defect (XRM, 9 μm pixel size) at three different locations (**a**) at the location with the deepest defect, (**b**) at the boundary location of the defect, and (**c**) at various locations of the defect [19].

For a faster evaluation of the test specimen's state, the version of the Sensor 3D training with the segmentation wizard toolbox was subsequently used to automatically label the 2014 slices of the CT scan. The 3D results of the initial test specimen state are shown in Figure 18a. The black 3D geometrical half cylinder represents the scanned specimen, and the spheres colored purple represent the defects. The Sensor 3D labeled the artifacts, the noise, and both ends of the specimen along the longitudinal edges as pores. This indicates that further training of the CNN was required to reduce noise.
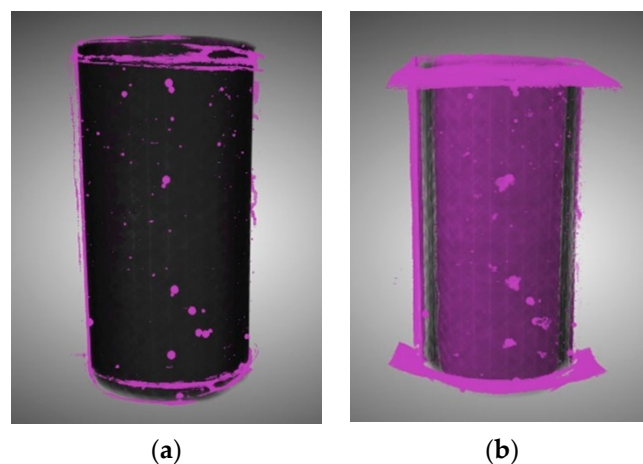

(**a**)   (**b**)

Figure 18. Defect detection (**a**) in the initial state and (**b**) after rain loading, adapted with permission from [19].

After loading the specimen with rain in the rain erosion test facility, the specimen was scanned again, and the same procedure was applied to the new data set. The results are displayed in Figure 18b. The effect of noise and ring artifacts is visible in this scan. Nevertheless, the defects were successfully located. The voids increased in size due to rain erosion. The trained CNN showed that the accuracy and training based on a handful of frames were sufficient for the segmentation of the whole data set. Another training strategy needs to be developed to ensure the robustness of the CNN. The training of neural

networks required a small amount of annotated data sets, so the biggest hurdle to using AI was overcome. With the help of the trained networks, the data analysis can be accelerated with modern hardware, especially with a powerful graphics card. A relevant aspect at this point is the use of cloud computing as an alternative to modernizing the existing hardware.

In addition to the computed tomographic measurements and AI evaluation, surface analysis using the fringe light projection method (3D profilometer) was carried out to generate an overview of the specimen surface and to document surface defects in their three-dimensional shape. The initial test specimen state is shown in Figure 19. Figure 19a shows a smooth surface based on the image recordings, which has a certain inhomogeneity in the form of an undefined waviness. This is also clearly evident from the 3D profilometer height representation in Figure 19b. In addition, individual defects introduced in the coating can be seen in the height image using slightly indicated local elevations on the surface, but not in the visual image.
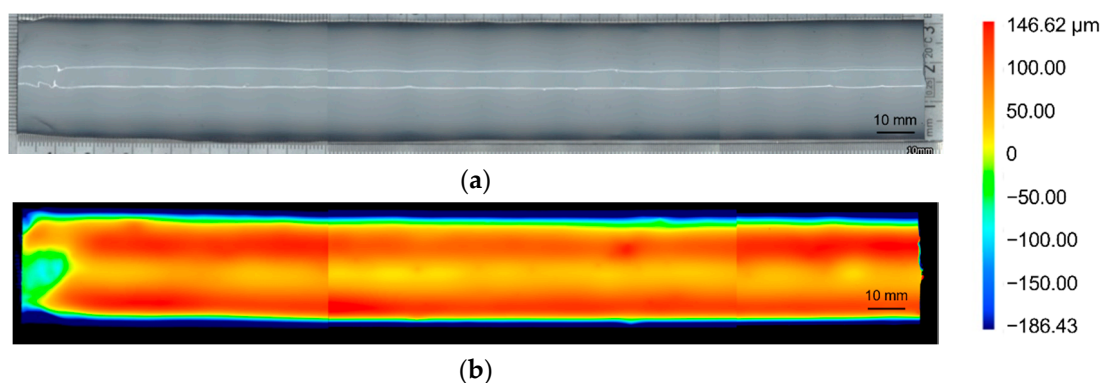

Figure 19. (**a**) Visual image and (**b**) 3D profilometer height image of a test specimen with voids in the coating before rain loading.

Figure 20 shows the damaged test specimen state after loading with rain. In both the visual image and the height image, the defects on the surface of the coating caused by rain erosion are visible. Small defects appear on the surface along the entire specimen, which is hypothesized to result from initially introduced defects since they weaken the material structure. Significant damage due to rain erosion is visible in the area of the marking hole of the GFRP specimen (about 1 cm to 1.5 cm from the left end of the specimen). In addition, a coating peeling is visible in the front area of the specimen (up to 3 cm from the left edge). These large-area coating peels are due to adhesion restrictions of the individual applied coating layers on this specimen.
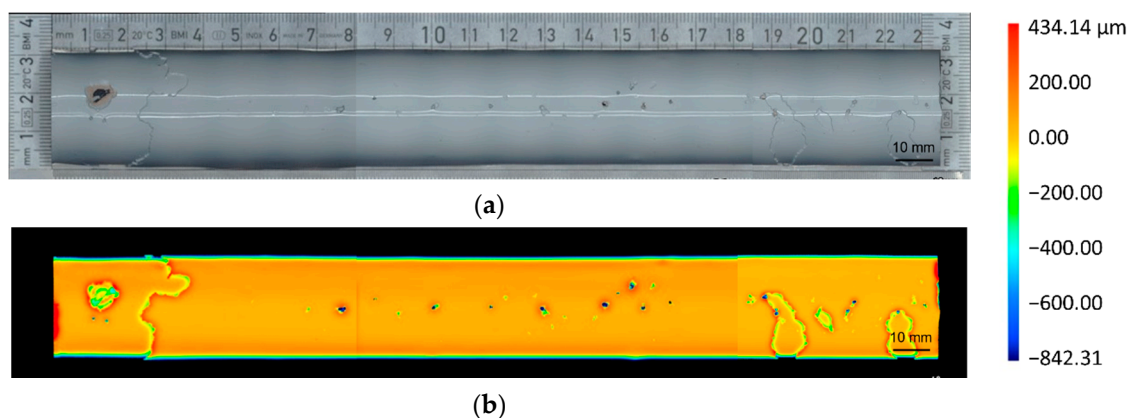

Figure 20. (**a**) Visual and (**b**) 3D profilometer height image of a whole test specimen with voids in the coating after rain loading.

In conclusion, the evaluated CT and XRM data results show that initial defects not visible from the outside are weak points where the material is destroyed at first, and the defects grow during rain loading. Furthermore, the surface defects appear to be smaller when observed from the outside as they are inside the specimen, so in both cases, a visual inspection of the leading edge of a GFRP rotor blade is not suitable for assessing the entire damage, as the full extent of the degraded area cannot be determined. Therefore, a measurement method for in-situ applications is necessary, which can visualize both the damaged state of the rotor blade leading edge as well as the damaged state beneath the surface.

3.3. Analysis of the Erosion Evolution Using Active Thermography

A feasibility study of thermographic measurements is carried out to show the potential for later in-situ monitoring. Figure 21 shows a specimen section's thermograms before and after rain exposure as an example.
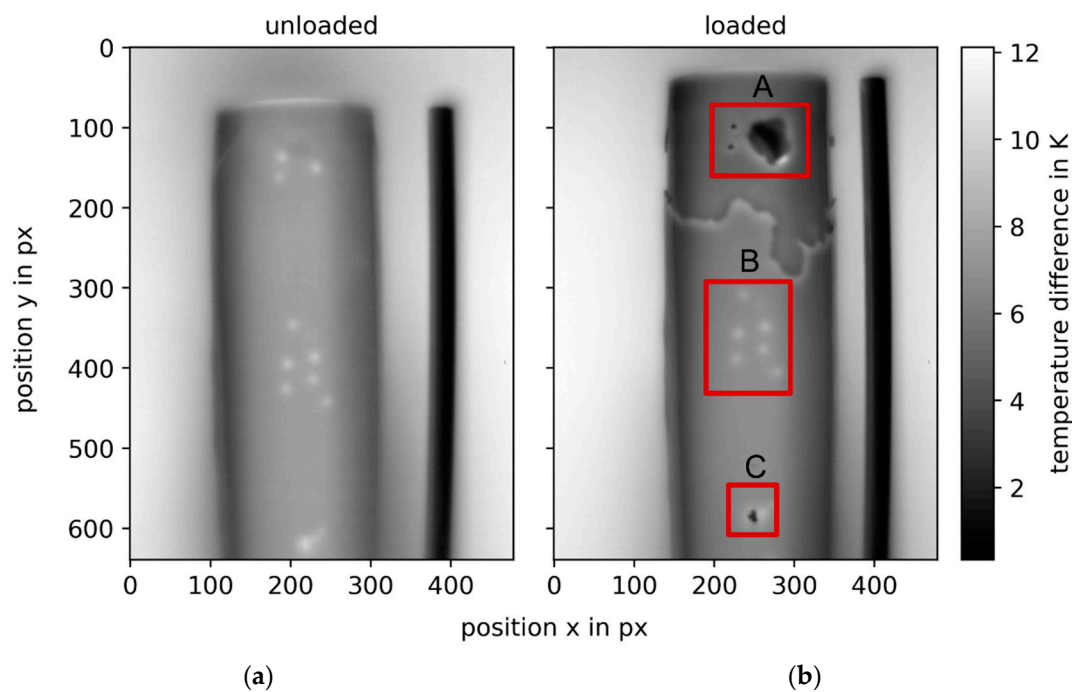

Figure 21. Thermogram of a specimen section with the environment at an excitation time of $t_{exc} = 10\,\mathrm{s}$; (**a**) unloaded condition; (**b**) loaded condition. The red boxes A–C show different defects; A: large surface damage, B: subsurface dafects, C: pinhole.

Before rain loading, the introduced defects appear as bright or hot spots on the specimen, see Figure 21a. Since the thermal conductivity of air with $0.0262\,\mathrm{W/(m \cdot K)}$ is significantly lower than the thermal conductivity of the coating with $0.2\,\mathrm{W/(m \cdot K)}$ (estimated value based on polyurethane as base material, since no data is available for the coating in this respect), the heat introduced during excitation accumulates in front of the defects. Here, the coating heats up more strongly than in areas without defects. The thermogram after rain loading shows evolved surface damages (A) in addition to sub-surface defects (B). The surface damages are indicated by lower temperatures or darker areas; see Figure 21b. Special attention should be paid to the pinhole in the center of the specimen at pixel position $y = 600\,\mathrm{px}$ (C). Here, according to the bright border area of the defect, the damage below the surface is larger than it is visible at the surface in a visual image.

For the validation of the thermographic measurement method, a comparison of the different measurement methods is shown in Figure 22.
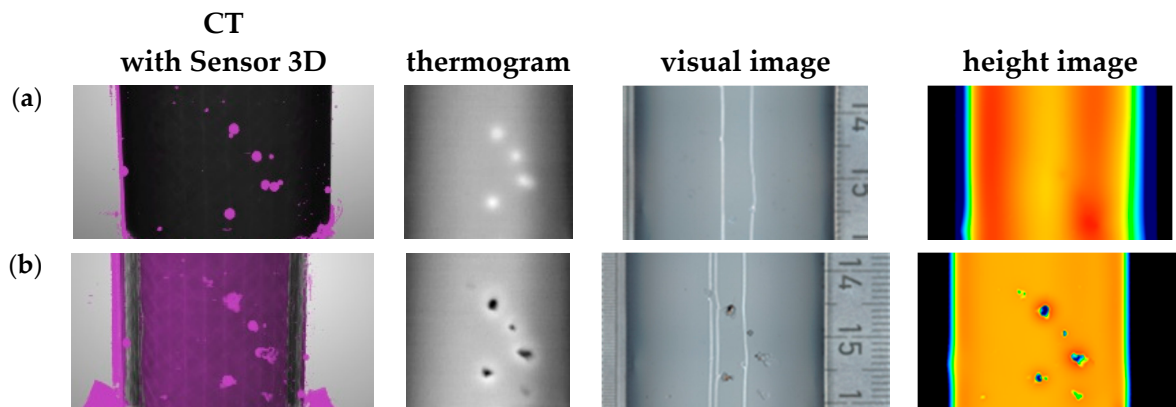
Figure 22. Result presentation of a section of a specimen with voids in the coating as a comparison between the applied measurement methods, including visual images, height images, thermography (normalized raw image), and the Sensor 3D segmentation results of the CT data, in (**a**) unloaded and (**b**) loaded condition.

Figure 22a shows the image section in the unloaded state. While no irregularities can be seen in the visual image and the 3D topography, the thermogram shows irregularities in the form of hot spots. These irregularities can also be seen in the CT. Since the specimen has inserted voids, it can be assumed that exactly these initial defects were detected. Therefore, the specimen's condition is not ideal, even if it appears to be so from the outside.

Figure 22b shows the same specimen section after a 4 h exposure to rain. In the visual image and the 3D profilometer, defects are now clearly visible on the surface of the specimen. In the thermogram, these defects can also be declared as surface defects in the form of dark spots. It is noticeable that the surface defects are surrounded by a bright border, which would mean that the defect under the surface is significantly larger than visible at the surface. A look at the CT image confirms that the defects have grown in size compared to before rain loading. Here, the defect size in the CT differs from the defect sizes in the visual images, indicating that the defects have also grown below the surface, which validates the thermographic results.

The investigations show that it is possible to generate realistic erosion damage in the laboratory. Furthermore, the experiments show that premature erosion starts from initial defects in the test specimen and then enlarges to different sizes after rain loading. The CT and the XRM measurements show that surface defects are often bigger than visible at the surface. The thermographic feasibility study shows the same results. Therefore, only visual inspection of the rotor blade is not sufficient for integrated condition assessment of rotor blade leading edges. Furthermore, the thermographic investigations show that not only sub-surface defects but also surface damage can be visualized in a single thermographic image, and an additional visual camera is unnecessary.

To conclude, the condition of a rotor blade's leading edge should therefore be inspected before it is used on a wind turbine. Active thermography, in particular, offers great potential as a measurement method since it is highly flexible compared to CT and can be used at various locations, including in the open field.

4. Conclusions and Outlook

Within this work, investigations were carried out to establish a correlation between initial defects in rotor-blade-leading-edge-like specimens and erosion damage after rain load to clarify the causes and mechanisms of premature damage. By modifying specimens that closely resemble the structure and the material of wind turbine rotor blade leading edges and impacting them in a rain erosion test facility, it was possible to generate realistic erosion damage in the laboratory. The investigations have shown that erosion damage occurs preferentially in those areas of the specimens that were already damaged before the rain load, for example, in the form of voids in the coating. Early erosion damage is

thus due, among other things, to a non-ideal specimen condition or non-ideal condition of the rotor blade leading edge. The experiments with different measurement methods like CT and XRM show that the surface erosion damage below the surface is larger than what the surface damage would suggest. These results were obtained with the measurement method of active thermography as well. In addition, thermographic measurements can detect defects below the surface and on the surface within one image. Thus, in contrast to simple surface analysis like visual inspection, the entire damaged state of the specimen can be visualized and validated by the CT examinations. The feasibility study of thermography thus shows promising potential for future in-situ applications.

In the further course of the investigations, the defect formation will be examined in more detail through cyclic erosion tests and the performance of intermediate examinations to make statements about the damage growth and to enhance our understanding of damage mechanisms. Furthermore, a quantitative evaluation of the damage condition in the different erosion stages is planned.

Author Contributions: Conceptualization, F.J., M.S. (Michael Sorg), A.F., O.F., E.A.A., A.K., M.S. (Mareike Schlag) and C.T.; methodology, F.J., A.F., O.F., A.K. and C.T.; software, F.J., O.F. and E.A.A.; validation, F.J., O.F., E.A.A., A.K. and C.T.; formal analysis, F.J., O.F., E.A.A., A.K. and C.T.; investigation, F.J., O.F., E.A.A., A.K., C.T. and C.L.; resources, F.J., O.F., A.K. and C.T.; data curation, F.J., O.F., A.K. and C.T.; writing—original draft preparation, F.J., O.F., E.A.A., A.K. and C.L.; writing—review and editing, M.S. (Michael Sorg), A.F., B.M., M.S. (Mareike Schlag) and A.H.; visualization, F.J., O.F., E.A.A., A.K., C.T. and C.L.; supervision, M.S. (Michael Sorg), A.F., M.S. (Mareike Schlag), B.M. and A.H.; project administration, F.J., O.F., A.K. and C.T.; funding acquisition, M.S. (Michael Sorg), O.F., C.T. and M.S. (Mareike Schlag). All authors have read and agreed to the published version of the manuscript.

Institutional Review Board Statement: Not applicable.

Informed Consent Statement: Not applicable.

Data Availability Statement: Not applicable.

Conflicts of Interest: The authors declare no conflict of interest.

Nomenclature

The following nomenclature is used in this manuscript:

AI	artificial intelligence
CT	X-Ray Computed Tomography
CNN	convolutional neural network
GFRP	glass fiber-reinforced plastic
ROI	region of interest
XRM	X-Ray Microscopy
t_{exc}	excitation time in [s]

References

1. Keegan, M.H.; Nash, D.H.; Stack, M.M. On erosion issues associated with the leading edge of wind turbine blades. *J. Phys. D Appl. Phys.* **2013**, *46*, 383001. [CrossRef]
2. 3M. Studie von 3M zeigt erstmals den Zusammenhang von Erosion und Effizienz bei Windkraftanlagen. *Windkraft-Journal*, 09.06. 2011. Available online: http://www.windkraft-journal.de/2011/09/06/3513/3513 (accessed on 4 November 2022).

3. DIN (Deutsches Inistut für Normung)—Normenausschuss Beschichtungsstoffe und Beschichtungen (NAB). *Beschichtungen an Rotorblättern für Windenergieanlagen (NA 002-00-16 AA)*; DIN: Berlin, Germany, 2018.
4. Oehler, H.; Bargmann, M.; Lellinger, D.; Alig, I. Warum ist der Lack ab? *Farbe und Lack* **2011**, *1*.
5. Cortés, E.; Sánchez, F.; O'Carroll, A.; Madramany, B.; Hardiman, M.; Young, T.M. On the Material Characterisation of Wind Turbine Blade Coatings: The Effect of Interphase Coating-Laminate Adhesion on Rain Erosion Performance. *Materials* **2017**, *10*, 1146. [CrossRef] [PubMed]
6. Krumm, M.; Sauerwein, C.; Hämmerle, V.; Oster, R.; Diewel, B.; Sindel, M. Capabilities and Application of Specialized Computed Tomography Methods for the Determination of Characteristic Material Properties of Fiber Composite Components. In Proceedings of the 4th Conference on Industrial Cpmputed Tomography (iCT), Wels, Austria, 19–21 September 2012.
7. Hanke, R. Computertomographie in der Materialprüfung: Stand der Technik und aktuelle Entwicklungen. In *DGZfP-Jahrestagung*; DGZfP (Deutsche Gesellschaft für zerstörungsfreie Prüfung e.V.): Erfurt, Germany, 2010.
8. Garcea, S.C.; Wang, Y.; Withers, P.J. X-ray computed tomography of polymer composites. *Compos. Sci. Technol.* **2018**, *156*, 305–319. [CrossRef]
9. Focke, O.; Bostan, L.; Gaitzsch, R.; Koerdt, M.; Jansen, F.; Meijer, F.; Miene, A.; Hesselbach, J.; Lührs, H.; Dimassi, A.; et al. Multiscale non-destructive investigations of aeronautic structures: From a single fiber to complex shaped fiber-reinforced composites. In Proceedings of the 8th Conference on Industrial Computed Tomography, Wels, Austria, 6–9 February 2018.
10. Nash, D.; Leishman, G.; Mackie, C.; Dyer, K.; Yang, L. A Staged Approach to Erosion Analysis of Wind Turbine Blade Coatings. *Coatings* **2021**, *11*, 681. [CrossRef]
11. Mishnaevsky, L.; Fæster, S.; Mikkelsen, L.P.; Kusano, Y.; Bech, J.I. Micromechanisms of leading edge erosion of wind turbine blades: X-ray tomography analysis and computational studies. *Wind Energy* **2019**, *23*, 547–562. [CrossRef]
12. Bang, H.-T.; Park, S.; Jeon, H. Defect identification in composite materials via thermography and deep learning techniques. *Compos. Struct.* **2020**, *246*, 112405. [CrossRef]
13. Badran, A.; Marshall, D.; Legault, Z.; Makovetsky, R.; Provencher, B.; Piché, N.; Marsh, M. Automated segmentation of computed tomography images of fiber-reinforced composites by deep learning. *J. Mater. Sci.* **2020**, *55*, 16273–16289. [CrossRef]
14. Ronneberger, O.; Fischer, P.; Brox, T. U-Net: Convolutional Networks for Biomedical Image Segmentation. *arXiv* **2015**, arXiv:1505.04597.
15. Jensen, F.; Terlau, M.; Sorg, M.; Fischer, A. Active Thermography for the Detection of Sub-Surface Defects on a Curved and Coated GFRP-Structure. *Appl. Sci.* **2021**, *11*, 9545. [CrossRef]
16. Colombo, C.; Bhujangrao, T.; Libonati, F.; Vergani, L. Effect of delamination on the fatigue life of GFRP: A thermographic and numerical study. *Compos. Struct.* **2019**, *218*, 152–161. [CrossRef]
17. Katunin, A.; Wronkowicz-Katunin, A.; Wachla, D. Impact damage assessment in polymer matrix composites using self-heating based vibrothermography. *Compos. Struct.* **2019**, *214*, 214–226. [CrossRef]
18. Meola, C.; Carlomagno, G.M. Infrared thermography to evaluate impact damage in glass/epoxy with manufacturing defects. *Int. J. Impact Eng.* **2014**, *67*, 1–11. [CrossRef]
19. Krenz, A.; Tornow, C.; Focke, O.; Abi Aoun, E.; Jensen, F. *Systematische Ursachenforschung von Erosionsschäden an Windenergieanlagen Mittels Computertomographie (XRM) als Basis zur Schadensminimierung von Serciveoptimierung (SUrfErCut): Schlussbericht vom 30.09.2022*; Universität Bremen: Bremen, Germany, 2022.
20. DNV-GL (Det Norske Veritas and Germanischer Lloyd). *Evaluation of Erosion and Delamination for Leading Edge Protection Systems of Rotor Blades*; DNV-GL-RP-0573; DNV-GL: Bærum, Norway, 2020.
21. Provencher, B.; Piché, N.; Marsh, M. Simplifying and Streamlining Large-Scale Materials Image Processing with Wizard-Driven and Scalable Deep Learning. *Microsc. Microanal.* **2019**, *25*, 402–403. [CrossRef]
22. Object Research System (ORS) Inc. *Dragonfly*; Object Research System (ORS) Inc.: Montreal, QC, Canada, 2020.
23. Novikov, A.; Major, D.; Wimmer, M.; Lenis, D.; Bühler, K. Deep Sequential Segmentation of Organs in Volumetric Medical Scans. *IEEE Trans. Med. Imaging* **2019**, *38*, 1207–1215. [CrossRef] [PubMed]
24. Almond, D.P.; Angioni, S.L.; Pickering, S.G. Long pulse excitation thermographic non-destructive evaluation. *NDT E Int.* **2017**, *87*, 7–14. [CrossRef]
25. Wang, Z.; Tian, G.; Meo, M.; Ciampa, F. Image processing based quantitative damage evaluation in composites with long pulse thermography. *NDT E Int.* **2018**, *99*, 93–104. [CrossRef]